Robust Recovery of Temporal Overlap Between Network Activity Using Transient-Informed Spatio-Temporal Regression

Daniela M. Zöller, Thomas A. W. Bolton, *Student Member, IEEE*, Fikret Işık Karahanoğlu, Stephan Eliez, Marie Schaer, and Dimitri Van De Ville, *Senior Member, IEEE*

***Abstract*— Functional magnetic resonance imaging is a non-invasive tomographic imaging modality that has provided insights into system-level brain function. New analysis methods are emerging to study the dynamic behavior of brain activity. The innovation-driven co-activation pattern (iCAP) approach is one such approach that relies on the detection of timepoints with a significant transient activity to subsequently retrieve spatially and temporally overlapping large-scale brain networks. To recover temporal profiles of the iCAPs for further time-resolved analysis, spatial patterns are fitted back to the activity-inducing signals. In this crucial step, spatial dependences can hinder the recovery of temporal overlapping activity. To overcome this effect, we propose a novel back-projection method that optimally fits activity-inducing signals given a set of transient timepoints and spatial maps of iCAPs, thus taking into account both spatial and temporal constraints. Validation on simulated data shows that transient-based constraints improve the quality of fitted time courses. Further evaluation on experimental data demonstrates that overfitting and underfitting are prevented by the use of optimized spatio-temporal constraints. Spatial and temporal properties of resulting iCAPs support that brain activity is characterized by the recurrent co-activation and co-deactivation of spatially overlapping large-scale brain networks. This new approach opens new avenues to explore the brain's dynamic core.**

***Index Terms*— fMRI, dynamic functional connectivity, innovation-driven co-activation patterns, large-scale brain network dynamics, spatio-temporal regression.**

Manuscript received June 12, 2018; accepted July 30, 2018. Date of publication September 4, 2018; date of current version December 28, 2018. This work was supported in part by the National Center of Competence in Research SYNAPSY (the Synaptic Bases of Mental Diseases), SNSF, under Grant 51AU40_125759 and Grant 51NF40_158776 and in part by the Bertarelli Foundation. The work of S. Eliez was supported by the Swiss National Science Foundation under Grant 32473B_121966, Grant 234730_144260, and Grant 145250. The work of M. Schaer was supported by the Swiss National Science Foundation under Grant 163859. *(Corresponding author: Daniela M. Zöller.)*

D. M. Zöller is with the Medical Image Processing Laboratory, Institute of Bioengineering, École Polytechnique Fédérale de Lausanne, 1015 Lausanne, Switzerland, and also with the Developmental Imaging a Psychopathology Laboratory, Departments of Radiology and Medical Informatics and Psychiatry, University of Geneva, 1211 Geneva, Switzerland (e-mail: daniela.zoller@epfl.ch).

T. A. W. Bolton and D. Van De Ville are with the Medical Image Processing Laboratory, Institute of Bioengineering, École Polytechnique Fédérale de Lausanne, 1015 Lausanne, Switzerland, and also with the Department of Radiology and Medical Informatics, University of Geneva, 1211 Geneva, Switzerland.

F. I. Karahanoğlu is with the Martinos Center for Biomedical Imaging, Massachusetts General Hospital, Boston, MA 02129 USA, and also with the Department of Psychiatry, Harvard Medical School, Boston, MA 02215 USA.

S. Eliez and M. Schaer are with the Developmental Imaging an Psychopathology Laboratory, Department of Psychiatry, University of Geneva, 1211 Geneva, Switzerland.

This paper has supplementary downloadable material available at http://ieeexplore.ieee.org, provided by the author.

Color versions of one or more of the figures in this paper are available online at http://ieeexplore.ieee.org.

Digital Object Identifier 10.1109/TMI.2018.2863944

I. Introduction

During the past two decades, investigations using resting-state functional magnetic resonance imaging (fMRI) found evidence that normal brain function is characterized by fluctuations in the activity of large-scale brain networks, that is, of distributed sets of brain regions that are coherently fluctuating [1], [2]. Functional connectivity (FC) measures statistical interdependency between two time courses, conventionally by pairwise correlation. Another widely used methodology to study networked brain activity is independent component analysis (ICA) that relies on a surrogate measure for statistical independence [3], [4]. While FC and ICA most commonly assume stationarity over the whole resting-state run, recent findings suggest that it is meaningfully variable over time [5], and that the consideration of dynamic features is promising when studying brain function and its alterations in mental disorders [6], [7].

Multiple approaches exist for the retrieval and analysis of dynamic FC (dFC) networks; for extensive reviews see [7]–[9]. Sliding-window approaches track dynamic changes by restraining the computation of second-order correlation to a temporal interval which is gradually shifted over time [5], [10]–[12]. However, this approach is limited to the detection of FC changes at much slower rate than the sampling rate, whereas actual FC changes might take place at a faster rate. Several novel approaches have been proposed to go beyond sliding-window correlations and detect rapid changes in FC. Window-less ICA-based approaches propose to analyze the dynamics of independent components (ICs) using for example dictionary learning [13] or hidden Markov models [14]. In parallel, so-called first-order techniques

0278-0062 © 2018 IEEE. Translations and content mining are permitted for academic research only. Personal use is also permitted, but republication/redistribution requires IEEE permission. See http://www.ieee.org/publications_standards/publications/rights/index.html for more information.

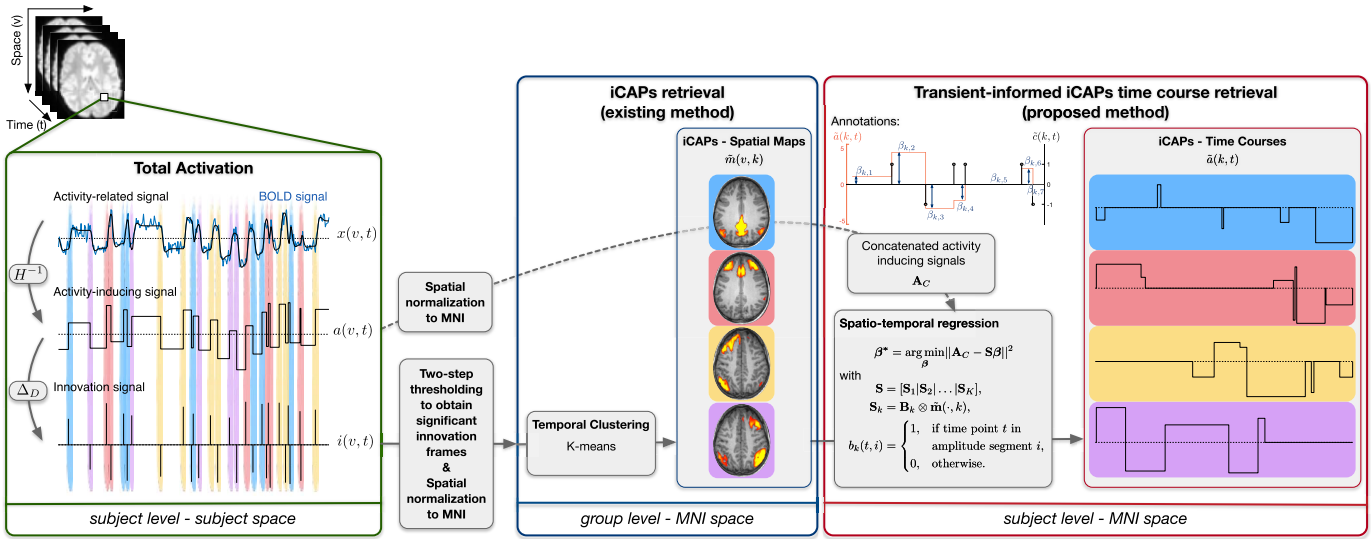

Fig. 1. Schematic representation of the key components related to this work. The total activation framework (green box) provides innovation signals that encode transients. Then, iCAPs are retrieved by temporal clustering (blue box). Finally, we propose to recover the iCAPs-related activity-inducing signals using a new spatio-temporal regression approach (red box).

were developed, which identify fMRI frames that reflect key activity patterns in a point process analysis (PPA); e.g., by the detection of significantly strong activity in a seed region [15]. An extension of this approach applies temporal clustering on the selected frames to establish whole brain co-activation patterns (CAPs) occurring during those moments defined by a single seed's time series [16]. This seed-driven approach has further been extended for the whole-brain by including multiple seeds [17], [18].

Yet another approach has been to incorporate a change point detector to retrieve timepoints of significant transient activity; e.g., by identifying moments of maximal brain-state changes [19] or using derivatives [20]–[22]. Combining this idea with principles from CAP analysis, temporal clustering on significant transient timepoints yields innovation-driven CAPs (iCAPs) [23], which are illustrated in Fig. 1. These spatial patterns reminiscent for known functional networks are simultaneously *transitioning* rather than simultaneously *activating*, which provides unique advantages over other commonly used methods. ICA, for instance, imposes statistical independence either in space or in time and CAPs are per definition temporally segregated, with only one active CAP at a time. This flexibility in spatial and temporal representation makes iCAPs thus especially well suited for the investigation of the resting state where there is no prior information on timing of brain-state transitions and strong temporal overlap of functional components is likely given the hemodynamic nature of fMRI signals [6].

To precisely detect timepoints with transient activity, fMRI signals must be deconvolved from the hemodynamic response function (HRF). For this the total activation (TA) framework has been developed [24] (Fig. 1, green box), resulting into the activity-inducing signals. The derivative of activity-inducing signals, so-called innovation signals, are then temporally clustered into representative spatial patterns (Fig. 1, blue box). To obtain the activation time courses of the iCAPs, these spatial patterns are then fitted back to the activity-inducing signals.

Even though the possibility of spatial overlap is one of the key advantages of iCAPs, spatial dependence may hinder the recovery of temporal overlap in the regression procedure. Here, we address this issue and propose a new back-projection method to optimally fit activity-inducing signals given a set of transient timepoints and spatial maps of iCAPs. This approach takes into account both spatial and temporal constraints to retrieve iCAPs' temporal profiles, which gives access to their dynamics for further analysis.

In the following, we first briefly describe the TA and iCAPs pipeline. Then, we introduce our novel transient-informed spatio-temporal regression approach and validate the proposed method on simulated data. Finally, we evaluate it on experimental data to demonstrate the benefits of our approach.

II. Methods

A. Methods Implementation

An open repository containing the full code for the application of processing steps including TA, iCAPs retrieval and spatio-temporal regression is available at https://c4science.ch/source/iCAPs.git.

B. Total Activation and Innovation-Driven Co-Activation Patterns

1) Total Activation: The TA framework uses spatio-temporal regularization to deconvolve the fMRI signal from the HRF (see Fig. 1, green box). The signal model explains the measured fMRI signal $y(v,t)$ as a convolution of an underlying neural signal $a(v,t)$, assumed to be block-type at the timescale of fMRI (that is seconds), with the HRF $h(t)$, and is corrupted by additive white Gaussian noise $\epsilon(v,t)$:

$$y(v,t) = (h \star a)(v,t) + \epsilon(v,t).$$

Here and throughout, the index $v \in \mathbb{N}$ indicates the voxel with $1 \leq v \leq N_v$, N_v being the total number of grey matter voxels, and index $t \in \mathbb{N}$ indicates the timepoint with $1 \leq t \leq N_t$, N_t being the total number of timepoints. Using vector notation $\mathbf{y}(v, \cdot) = [y(v, 1), \ldots, y(v, N_t)]$, we write

$$\mathbf{y}(v, \cdot) = (\mathbf{h} \star \mathbf{a})(v, \cdot) + \boldsymbol{\epsilon}(v, \cdot),$$

where $\boldsymbol{\epsilon}$ is distributed as $\mathcal{N}(0, \mathbf{I}_{N_t}\sigma_v^2)$, where $\mathbf{I}_{N_t}$ is an $N_t \times N_t$ identity matrix. We designate $\mathbf{x} = \mathbf{h} \star \mathbf{a}$ the *activity-related* signal at voxel v, and $\mathbf{a}$ its *activity-inducing* signal. The complete data matrix of activity-related signals is denoted as $\mathbf{X} \in \mathbb{R}^{N_v \times N_t}$ and the fMRI signal matrix $\mathbf{Y} \in \mathbb{R}^{N_v \times N_t}$, see Table I for an overview of the notations.

Then, as illustrated in Fig. 1 (green box), the spatio-temporal regularization problem can be written as

$$\mathbf{X}^* = \arg\min_{\mathbf{X}} \frac{1}{2}||\mathbf{Y} - \mathbf{X}||_F^2 + \mathcal{R}_T(\mathbf{X}) + \mathcal{R}_S(\mathbf{X}),$$

where

$$\mathcal{R}_T(\mathbf{X}) = \sum_{v=1}^{N_v} \lambda_T(v) \sum_{t=1}^{N_t} |\Delta_L\{\mathbf{x}(v, \cdot)\}[t]|,$$

$$\mathcal{R}_S(\mathbf{X}) = \lambda_S \sum_{t=1}^{N_t} \sum_{v=1}^{N_v} \sqrt{\sum_{u \in \mathcal{S}(v)} (x(v, t) - x(u, t))^2}.$$

Here, $\lambda_T(v)$ is the temporal regularization parameter at voxel v, and λ_S is the spatial regularization parameter, which is the same at every timepoint t. The differential operator $\Delta_L = \Delta_D H^{-1}$ combines HRF deconvolution H^{-1} and derivative Δ_D, and $\mathcal{S}(v)$ denotes the surrounding neighbors of voxel v. The temporal regularization term $\mathcal{R}_T(\mathbf{X})$ imposes sparsity on the innovation signal $\mathbf{i}(v, \cdot) = \Delta_L\{\mathbf{x}(v, \cdot)\}$; i.e., on the derivative of the activity-inducing signal, and thereby favors a piecewise-constant activity-inducing block signal $\mathbf{a}(v, \cdot)$. The spatial regularization term $\mathcal{R}_S(\mathbf{X})$ promotes localized activations that are smooth in space [25]. The HRF $h(t)$ is modeled by first-order Volterra series approximation of the balloon model [26], [27] and is assumed to be constant across the whole brain. For more details on the TA implementation, we refer to [24], [25], and [28].

In this study, TA was applied separately for every subject on preprocessed fMRI data in subject space.

2) Innovation-Driven Co-Activation Patterns: After regularized deconvolution of the BOLD signal, K-means clustering is applied to innovation frames to retrieve spatial patterns of simultaneously transitioning voxels [23]. First, positive and negative innovations are split into two separate frames $\mathbf{i}_P(\cdot, t)$ and $\mathbf{i}_N(\cdot, t)$, where the sign of negative innovation frames is flipped. Then, significant transient frames were determined using a two-step thresholding approach: in the first step (temporal thresholding), the null distribution of every subject's innovation signal was determined by running TA on a phase-randomized surrogate dataset, and a subject-specific threshold at a 5 %-95 % confidence interval was applied. In the second step (spatial thresholding), an innovation frame was considered significant if at least 5% of all considered voxels showed a significant innovation. With these thresholding parameters, 81.8 ± 9.1 % of positive and 79.1 ± 10.3 % of negative frames were above threshold. Overall, 99.8 ± 0.4 % of the innovation frames showed at least a significant positive or negative innovation (or both events together). After thresholding, innovation frames were spatially normalized to Montreal Neurological Institute (MNI) space using Diffeomorphic Anatomical Registration using Exponentiated Lie algebra (DARTEL) [29] (see also subsection III-B).

TABLE I
OVERVIEW OF NOTATIONS. SIGNALS OBTAINED FOLLOWING THE GENERATION OF THE iCAPs ARE MARKED WITH A TILDE

Symbol	Description
$t \in \mathbb{N}$	timepoint (frame) index
$v \in \mathbb{N}$	voxel index
$k \in \mathbb{N}$	cluster index
$y(v, t)$; $\mathbf{Y} \in \mathbb{R}^{N_v \times N_t}$	measured voxelwise BOLD signal
$x(v, t)$; $\mathbf{X} \in \mathbb{R}^{N_v \times N_t}$	voxelwise activity-related signal
$a(v, t)$; $\mathbf{A} \in \mathbb{R}^{N_v \times N_t}$	voxelwise activity-inducing signal
$\mathbf{A}_C \in \mathbb{R}^{N_t N_v \times 1}$	concatenated activity-inducing signal
$i(v, t)$; $\mathbf{I} \in \mathbb{R}^{N_v \times N_t}$	voxelwise innovation/transient signal
$\tilde{m}(v, k)$; $\tilde{\mathbf{M}} \in \mathbb{R}^{N_v \times K}$	iCAP spatial maps
$\tilde{a}(k, t)$; $\tilde{\mathbf{A}} \in \mathbb{R}^{K \times N_t}$	iCAP-wise activity-inducing signal
$\tilde{c}(k, t) \in \{-1, 0, 1\}$	iCAP-wise cluster assignment

Then, spatially normalized, significant innovation frames of all subjects were concatenated and temporal K-means clustering was applied at the group level with cosine distance as similarity measure (see Fig. 1, blue box). The group level spatial maps $\tilde{\mathbf{m}}(\cdot, k) = [\tilde{m}(1, k), \ldots, \tilde{m}(N_v, k)]^\top$ of each iCAP, $k \in 1, \ldots, K$, were retrieved by averaging the innovation frames of every cluster, after normalizing each frame to unit Euclidean length. In what follows, signals obtained following the generation of the iCAPs are marked with a tilde.

C. Consensus Clustering

In order to determine the best number of clusters, we employed consensus clustering [30], a resampling-based approach which applies K-means clustering on a subsample of the data and calculates the *consensus matrix* $\mathcal{M}$. Every element $\mathcal{M}(f_1, f_2)$ indicates the fraction of all subsamples for which two frames f_1 and f_2 are clustered together. The optimum cluster number can then be obtained by visual observation of the ordered matrix $\mathcal{M}$, as well as of the cumulative distribution function (CDF) of $\mathcal{M}$ and its area under the curve (AUC) for different values of K. See [30] for more details on the methods for clustering selection. Here, we applied consensus clustering for $K \in [10, 25]$ using 10 random subsamples for every K. Each subsample included the significant innovations of 45 (80 %) randomly selected subjects, and K-means was computed for 10 random initializations. To obtain the final clustering result, we applied K-means clustering with the optimum K on the entire dataset and kept the optimal result from 50 random initializations.

D. Time Course Recovery

In what follows, subject level iCAPs' time courses are either identified with the conventional *unconstrained spatial regression* approach or with our novel *transient-informed spatio-temporal regression* approach. The former treats every timepoint independently and only depends on spatial information, while the latter incorporates both spatial and temporal information.

1) Unconstrained Spatial Regression: In the conventional iCAPs framework [23], time-dependent amplitudes $\tilde{\mathbf{a}}(\cdot,t) = [\tilde{a}(1,t),\ldots,\tilde{a}(K,t)]^\top$ at timepoint t are retrieved by back-projection of the K group level spatial maps $\tilde{\mathbf{M}} \in \mathbb{R}^{N_v \times K} = [\tilde{\mathbf{m}}(\cdot,1),\ldots,\tilde{\mathbf{m}}(\cdot,K)]$ onto the activity-inducing signal $\mathbf{a}(\cdot,t)$ of each subject. Positive and negative transients are fitted separately to minimize the effect of spatial linear dependence, and the final time courses are defined as the sum of positive and negative fitted amplitudes, $\tilde{a}_P$ and $\tilde{a}_N$:

$$\tilde{a}(k,t) = \tilde{a}_P(k,t) + \tilde{a}_N(k,t),$$

with

$$\tilde{\mathbf{a}}_P^*(\cdot,t) = \underset{\tilde{\mathbf{a}}_P(\cdot,t)}{\arg\min} ||\mathbf{a}(\cdot,t) - \tilde{\mathbf{M}}\tilde{\mathbf{a}}_P(\cdot,t)||^2 \text{s.t. } \tilde{a}_P(k,t) \in [0,\infty[,$$

and

$$\tilde{\mathbf{a}}_N^*(\cdot,t) = \underset{\tilde{\mathbf{a}}_N(\cdot,t)}{\arg\min} ||\mathbf{a}(\cdot,t) - \tilde{\mathbf{M}}\tilde{\mathbf{a}}_N(\cdot,t)||^2 \text{s.t. } \tilde{a}_N(k,t) \in]-\infty,0].$$

2) Transient-Informed Spatio-Temporal Regression: As mentioned before, the unconstrained spatial regression approach for extracting the time courses of iCAPs can be contaminated by spatial dependencies of their maps, since the latter can be spatially overlapping. The main purpose of this paper is to introduce an alternative improved method, in order to overcome this problem and obtain more plausible time courses.

In principle, the method restricts changes in iCAPs time courses to moments when the iCAP in question is known to transition significantly. Information on these innovation timings is taken from the K-means clustering in the iCAPs retrieval step. Then, the design matrix for the regression problem is constructed with one regressor for each block of constant activation. In the following, we outline the detailed steps of the design matrix construction for this spatio-temporal regression method, namely (i) definition of innovation timings based on K-means information, (ii) construction of an indicator matrix $\tilde{\mathbf{C}}$ with innovation timings of all K iCAPs, (iii) construction of a temporal design matrix $\mathbf{B}_k$ with one regressor per activity block of each iCAP $k = 1,\ldots,K$, (iv) construction of the spatio-temporal design matrix $\mathbf{S}$ that also incorporates spatial information of the iCAPs maps to group voxels, and (v) the explicit formulation of the resulting linear optimization problem. Fig. 2 shows the assumed model for iCAPs time courses and Fig. 3 shows a schematic representation of the spatio-temporal regression design.

a) Innovation timing definition: With hard cluster assignment of transient frames, only two iCAPs are allowed to transition at the same time (one positively and one negatively). In order to allow for more than one iCAP to change simultaneously, we determine innovation timings using a soft cluster assignment according to the cosine distances of each frame to the cluster center: let $d(k,t)$ be the cosine distance of innovation frame $\mathbf{i}(\cdot,t)$ to cluster $\tilde{\mathbf{m}}(\cdot,k)$. Then the frame $\mathbf{i}(\cdot,t)$ (i.e., a significant innovation at timepoint t) will be assigned to all clusters k for which

$$d(k,t) \leq \xi d_{min}(t),$$

where $d_{min}(t)$ is the minimum distance of frame $\mathbf{i}(\cdot,t)$ to any cluster and $\xi \geq 1$ is a tuning parameter. Note that $\xi = 1$ corresponds to the hard cluster assignment used during K-means clustering.

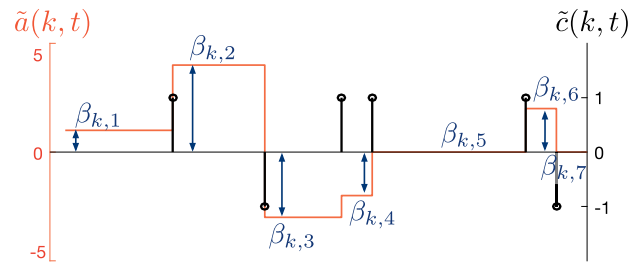

Fig. 2. Schematic representation of an example output iCAP time course $\tilde{a}(k,\cdot)$, the corresponding innovation indicator time course $\tilde{c}(k,\cdot)$, and the estimated amplitude values $\beta_{k,i}$.

b) Innovation timing indicator matrix: We then define the indicator matrix $\tilde{\mathbf{C}} \in \mathbb{R}^{K \times N_t}$ denoting the timepoints t with significant innovations for each iCAP k:

$$\tilde{c}(k,t) = \begin{cases} 1, & \text{if } d_P(k,t) \leq \xi d_{P,min}(t), \\ -1, & \text{if } d_N(k,t) \leq \xi d_{N,min}(t), \\ 0, & \text{otherwise,} \end{cases}$$

where d_P and d_N designate distances to positive and negative innovation frames $\mathbf{i}_P(\cdot,t)$ and $\mathbf{i}_N(\cdot,t)$, respectively. Further, we will denote the number of innovations for iCAP k by $N_{I_k} = \sum_{t=1}^{N_t} |\tilde{c}(k,t)|$, and the total number of innovations across all networks by $N_I = \sum_{k=1}^{K} N_{I_k}$.

c) Temporal design matrix: Our aim is to retrieve, for each iCAP k, a time course $\tilde{\mathbf{a}}(k,\cdot)$ that is piecewise constant between two nonzero values in $\tilde{\mathbf{c}}(k,\cdot)$. To do so, we must determine the optimal set of amplitudes $\beta_{k,i}$, $k = 1,\ldots,K$, $i = 1,\ldots,N_{I_k}+1$ between two significant transients (see Fig. 2 for a schematic representation). Note that there are $N_{I_k}+1$ coefficients to compute for each network.

For each iCAP, we construct the temporal design matrix $\mathbf{B}_k \in \mathbb{R}^{N_t \times N_{I_k}+1}$ that contains the activation segments separated by the innovations. If

$$\phi(t,k) = 1 + \sum_{\tau=1}^{t} |\tilde{c}(k,\tau)|$$

expresses the index of the segment at hand at time t, the elements $b_k(t,i)$ of $\mathbf{B}_k$ are

$$b_k(t,i) = \begin{cases} 1, & \text{if } \phi(t,k) = i, \\ 0, & \text{otherwise.} \end{cases}$$

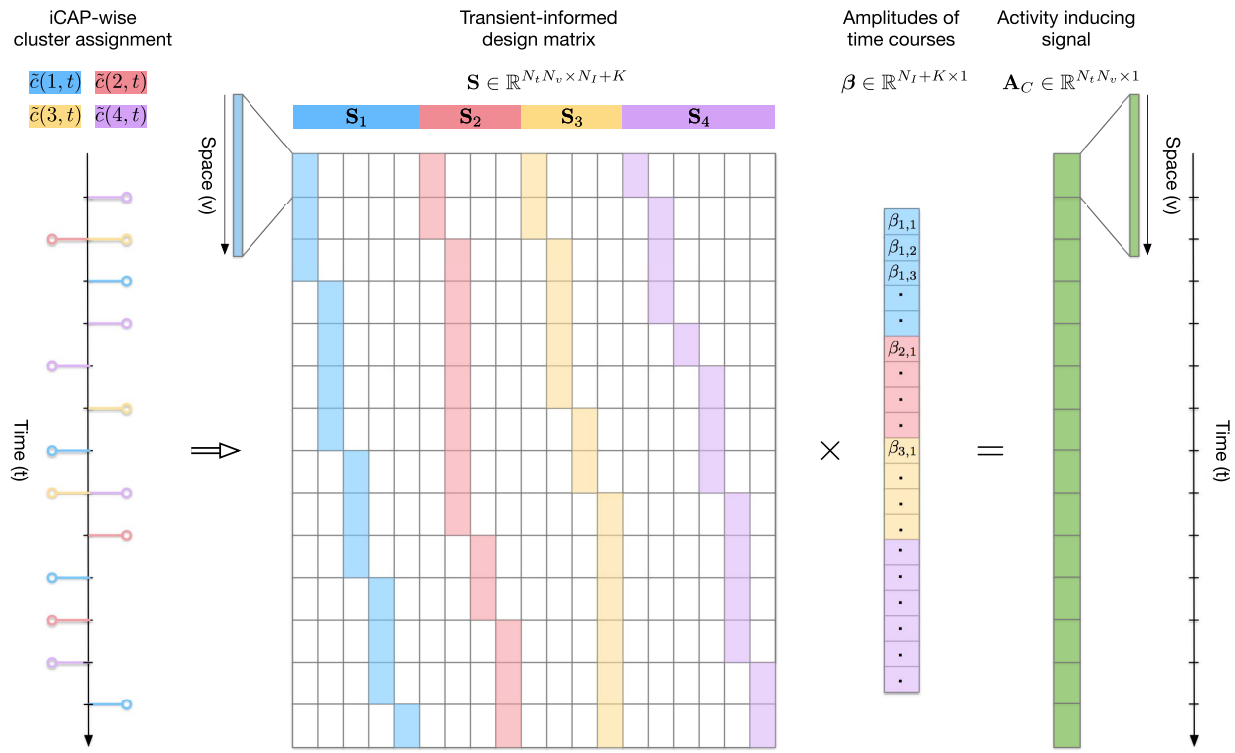

Fig. 3. Schematic representation of the transient-informed spatial regression optimization problem in the case of four iCAPs with $N_{I_1} = 4$, $N_{I_2} = 3$, $N_{I_3} = 3$ and $N_{I_4} = 5$ significant innovations, respectively, and $N_I = 15$ innovations in total. This example represents the most restrictive case of hard cluster assignment ($\xi = 1$) with at most two iCAPs changing simultaneously (one with positive and one with negative amplitude).

d) Spatio-temporal design matrix: Based on $\mathbf{B}_k$, we obtain the matrix $\mathbf{S}_k \in \mathbb{R}^{N_t N_v \times (N_{I_k}+1)}$ that contains the activation segments in the concatenated spatio-temporal space:

$$\mathbf{S}_k = \mathbf{B}_k \otimes \tilde{\mathbf{m}}(\cdot, k),$$

where $\otimes$ denotes the Kronecker product. Then, the combination of all spatio-temporal matrices $\mathbf{S}_k$ gives the final spatio-temporal design matrix $\mathbf{S} = [\mathbf{S}_1|\mathbf{S}_2|\ldots|\mathbf{S}_K]$.

v) Optimization problem: If we then define $\mathbf{A}_C \in \mathbb{R}^{N_t N_v \times 1}$ as the concatenated activity-inducing frames (see Fig. 3), the optimization problem becomes

$$\boldsymbol{\beta}^* = \arg\min_{\boldsymbol{\beta}} ||\mathbf{A}_C - \mathbf{S}\boldsymbol{\beta}||^2,$$

with the optimal amplitudes given by $\boldsymbol{\beta} \in \mathbb{R}^{N_I+K\times 1} = \left[\beta_{1,1}, \beta_{1,2}, \ldots, \beta_{1,N_{I_1}+1}, \beta_{2,1}, \ldots, \beta_{K,N_{I_K}+1}\right]^\top$. We then have the iCAP time course amplitudes $\tilde{a}(k,t) = \beta_{k,\phi(t,k)}$.

III. Data Description

A. Simulated Data

In order to evaluate our transient-informed regression approach, we applied both unconstrained regression and transient-informed regression to a simulated dataset.

To be realistic, we used the iCAPs maps $\tilde{\mathbf{M}} \in \mathbb{R}^{N_v \times K}$ that were retrieved from experimental data (see next paragraph). Then, to simulate block-like iCAP time courses $\tilde{\mathbf{A}}_{sim} \in \mathbb{R}^{K \times N_t}$, we first defined transient timings by a Poisson process. We simulated data for Poisson constants of 20, 15, 10 and 5 TR, as well as for Poisson parameters as estimated from experimental data by fitting a Poisson distribution to estimated innovation timings of each iCAP. In the latter case, Poisson parameters were ranging from 7.5 for iCAP 1 to 27 for iCAP 18. Simulated time courses for this setting will be called "realistic" in the following description. The number of simultaneously transitioning iCAPs was restricted to 3 for realistic simulations and 4, 6, 8, and 10 for Poisson constants 20, 15, 10 and 5, respectively. Simulated time courses were then created by setting the segment between two simulated innovations to a random amplitude drawn from a standard normal distribution.

To obtain simulated data at the voxel level, we take the simulated iCAPs time courses $\tilde{\mathbf{A}}_{sim}$ and generate voxel-wise activity-inducing signals

$$\mathbf{A}_{sim} = \tilde{\mathbf{M}}\tilde{\mathbf{A}}_{sim} + \boldsymbol{\epsilon},$$

with additive white Gaussian noise $\boldsymbol{\epsilon}$.

Activity-inducing signals were simulated without noise and at noise levels ranging from SNR = 10 dB to SNR = −10 dB. For quantitative evaluation, the root mean squared error (RMSE) between retrieved and ground truth iCAP time courses was computed, at each noise level, for 10 repetitions of the aforementioned simulation process.

B. Experimental Data

We included resting-state fMRI scans of 56 healthy subjects with no history of neurological or psychiatric disorders (M/F = 23/33, age = 16.85 ± 5.69, range: 6-29 years) who were recruited in the scope of the Geneva 22q11 deletion

syndrome cohort. From our initial sample of 80 subjects within the age range, we excluded 24 subjects based on a strict criterion for motion; i.e., framewise displacement [31] was computed for all frames and subjects were excluded if more than 10% of timepoints exceeded a threshold of 0.5 mm. Written informed consent was obtained from participants and their parents for subjects younger than 18 years old. The research protocols were approved by the Institutional Review Board of Geneva University School of Medicine.

Structural and functional MRI data were acquired at the Centre d'Imagerie BioMédicale (CIBM) in Geneva on a Siemens Trio (N = 42) and a Siemens Prisma (N = 14) 3 Tesla scanner. Anatomical images were acquired with a T1-weighted sequence of $0.86 \times 0.86 \times 1.1\, textmm^3$ volumetric resolution (192 slices, TR = 2500 ms, TE = 3 ms, acquisition matrix = 224 × 256, field of view = 22 cm^2, flip angle = 8°), and functional images with a T2*-weighted sequence of 8 minutes (voxel size = 1.84 × 1.84 × 3.2 mm^2, 38 slices, TR = 2400 ms, TE = 30 ms, flip angle = 85°). For the resting-state session, participants were asked to fixate a cross projected on a screen, let their minds wander while not thinking of anything in particular and not to fall asleep.

The fMRI scans were preprocessed using Statistical Parametric Mapping (SPM12, Wellcome Trust Centre for Neuroimaging, London, UK: http://www.fil.ion.ucl.ac.uk/spm/) and functions of the Data Processing Assistant for Resting-State fMRI (DPARSF) [32] and Individual Brain Atlases using Statistical Parametric Mapping (IBASPM) [33] toolboxes. The first five frames were excluded to ensure magnetization stability. Preprocessing steps included realignment, spatial smoothing with an isotropic Gaussian kernel of 6 mm full-width half-maximum, co-registration of structural scans to the functional mean and segmentation with the SPM12 *Segmentation* algorithm [34]. Average signals in the white matter and cerebrospinal fluid where regressed from the fMRI data. Then, frames with high motion were marked according to their framewise displacement [31] and if exceeding a threshold of 0.5 mm, were removed and filled in by cubic spline interpolation. Interpolation of removed frames is necessary as the implementation of TA deconvolution requires a constant sampling rate; i.e., a uniformly sampled HRF representation. TA was then applied in subject space, and the activity-inducing signals were subsequently normalized to MNI space using Diffeomorphic Anatomical Registration using Exponentiated Lie algebra (DARTEL) [29], followed by the aforementioned thresholding and clustering steps.

IV. Results

A. Consensus Clustering

We applied consensus clustering on all significant transients for cluster numbers K going from 10 to 25 (see Supplementary Fig. S1, available in the supplementary files/multimedia tab) and evaluated the results as proposed in [30]. According to the CDF and the relative increase of AUC curves, the optimum number of clusters was $K = 18$. Visual observation of the ordered consensus matrices confirmed this number, since sub-sampled frames were most stably assigned to the same cluster. In the following, we will thus investigate results for 18 clusters.

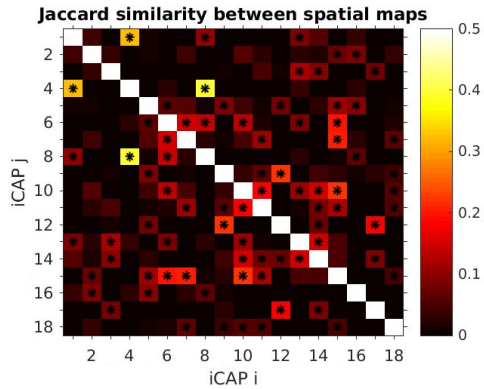

Fig. 4. Jaccard similarity index between spatial maps thresholded at a z-score of 1.5. Stars indicate significant values ($p < 0.01$ Bonferroni-corrected) determined with permutation testing.

B. Spatial Maps

Spatial maps of iCAPs that were retrieved from 56 healthy subjects are shown on Supplementary Fig. S2 (available in the supplementary files/multimedia tab). To evaluate recovered iCAPs in terms of spatial overlap, we computed the Jaccard similarity index between thresholded maps at a z-score of 1.5. The Jaccard index is defined as the intersection of two binary maps k_1 and k_2 divided by their union:

$$J_{k_1,k_2} = \frac{\sum_v [(\tilde{m}(v,k_1) > 1.5) \cap (\tilde{m}(v,k_2) > 1.5)]}{\sum_v [(\tilde{m}(v,k_1) > 1.5) \cup (\tilde{m}(v,k_2) > 1.5)]}.$$

Significant similarity values where determined by 1000 random permutations of iCAPs voxels. Fig. 4 shows the Jaccard similarity between the 18 iCAPs. There is significant spatial overlap between 40 out of the 153 possible combinations of iCAPs (26.14%). Highest similarity exists between iCAP 4 (primary visual) and iCAP 8 (precuneus/visual) and between iCAP 4 and iCAP 1 (higher visual).

These results show that there is high spatial overlap between iCAPs. In the following sections, we demonstrate that this spatial overlap can introduce artifacts in time course retrieval, which can be corrected with transient-informed regression.

C. Simulated Data: Goodness of Fit and Temporal Overlap

In order to compare unconstrained regression to transient-informed regression with known ground truth transients, we estimated time courses for different levels of noise and transient activity in the simulated data. Supplementary Table S1 (available in the supplementary files/multimedia tab) shows the quality of fit measured by the root mean squared errors (RMSE) for both regression methods. RMSE values are lowest for a scenario without noise and increase with higher noise levels.

Across all assessed cases, transient-informed regression performs significantly better in retrieving block-wise

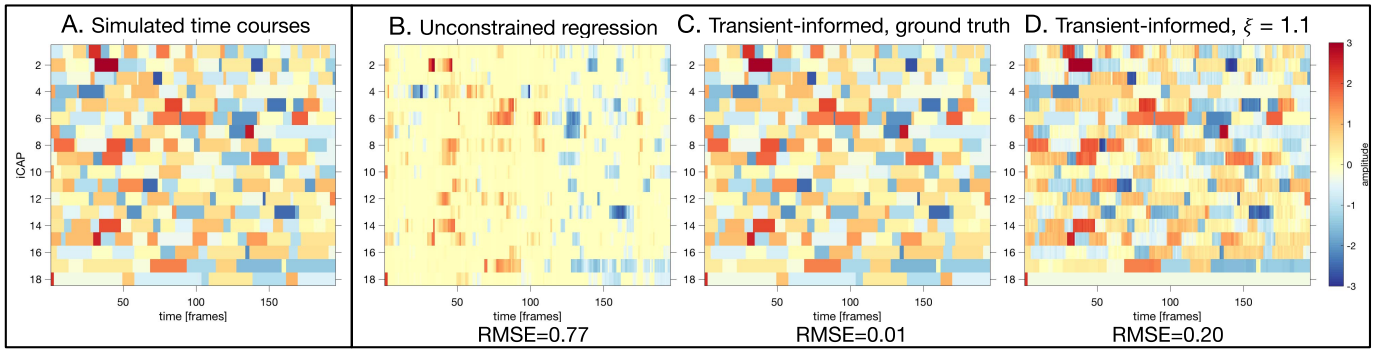

Fig. 5. A) Block-like time courses for transients with realistic Poisson constants from 7.5 (iCAP 1) to 27 (iCAP 18). B) to D) Time courses retrieved from activity-inducing signals, simulated with additive white Gaussian noise at SNR = 0 dB B) with unconstrained regression, C) with transient-informed regression and ground truth transient timings, and D) with transient-informed regression and soft cluster assignment at $\xi = 1.1$. Unconstrained regression misses many activity blocks, while transient-informed regression manages to retrieve the ground truth time courses almost perfectly.

time courses. Without noise, transient-informed regression with ground truth transients gives a perfect fit with RMSE close to zero. With increasing noise and with higher numbers of innovations (lower Poisson parameter), the RMSE increases slightly for transient-informed regression, but remains much lower than in unconstrained regression. Remarkably, even with very high noise and many innovations, transient-informed regression still performs more than 10 times better than unconstrained regression. We further evaluated regression with soft cluster assignment (see Supplementary Fig. S3, first row, available in the supplementary files/multimedia tab). Here, the RMSE converges towards values between 0.02 and 0.08, which is higher than the RMSE in case of regression with ground truth innovations, but still significantly smaller than in unconstrained regression. Even the worst fit for hard cluster assignment ($\xi = 1$) gives a lower RMSE than unconstrained regression.

Fig. 5 shows the exemplary case of simulated time courses with SNR = 0 dB and realistic Poisson constants, which demonstrates that unconstrained regression estimates are clearly off.

Temporal overlap between iCAPs was evaluated by thresholding time courses at an absolute z-score of 1 [23]. In simulated time courses, there are on average 5 to 6 simultaneously active iCAPs (see Supplementary Table S2, available in the supplementary files/multimedia tab). Temporal overlap is consistently underestimated in unconstrained regression, while with transient-informed regression the estimated overlap is very close to the ground truth.

In simulated ground truth time courses, iCAPs appear with the same sign in 52% to 55 % of all pairwise co-activations (i.e., either both iCAPs time courses positive or both negative, see Supplementary Table S3, available in the supplementary files/multimedia tab). In unconstrained regression, same-signed co-activations are highly overestimated. In fact, iCAPs appear almost always with the same sign if they are co-active (98% to 100 %). In transient-informed regression, estimated percentages of same-signed iCAPs appearances are again very close to the ground truth.

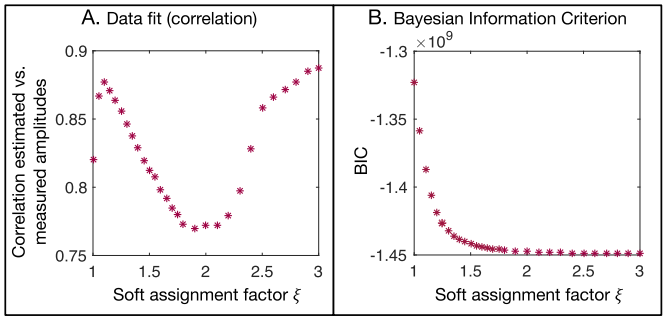

Fig. 6. Evaluation of soft assignment factors ξ from 1 (hard cluster assignment) to 3 (all iCAPs allowed to change at timepoints of significant transients).

D. Experimental Data: Optimal Soft Assignment Factor

Since in experimental data, the true innovations are not known, we use cluster assignments resulting from K-means to retrieve innovation timings (see subsection II-D). To determine the optimum factor ξ for soft cluster assignment of innovation frames, we tested the correspondence between estimated and measured transient amplitudes. Measured amplitudes were calculated by thresholding normalized iCAPs maps at a z-score of 1.5, and for each innovation frame $\mathbf{i}(\cdot, t)$, computing the average transient amplitude within the regions part of all iCAPs showing an innovation. The measured overall amplitude was defined as the sum of average amplitudes of all transitioning iCAPs, weighted by their distance to the respective cluster centers. We then correlated these measured innovation amplitudes with the estimated innovation amplitudes, computed from iCAPs time courses $\tilde{a}(\cdot, t)$ by summing innovation amplitudes across all transitioning iCAPs, again weighted by the distance to the respective cluster centers.

Fig. 6 shows the correlation for different values of the soft assignment factor ξ. The correlation first increases with higher ξ, reaches a local maximum of 0.88 at $\xi = 1.1$ and then decreases again. For $\xi > 1.9$ the correlation increases again due to overfitting to noise at these high innovation numbers. For high ξ, the results approach the unconstrained regression solution, for which the correlation between measured and

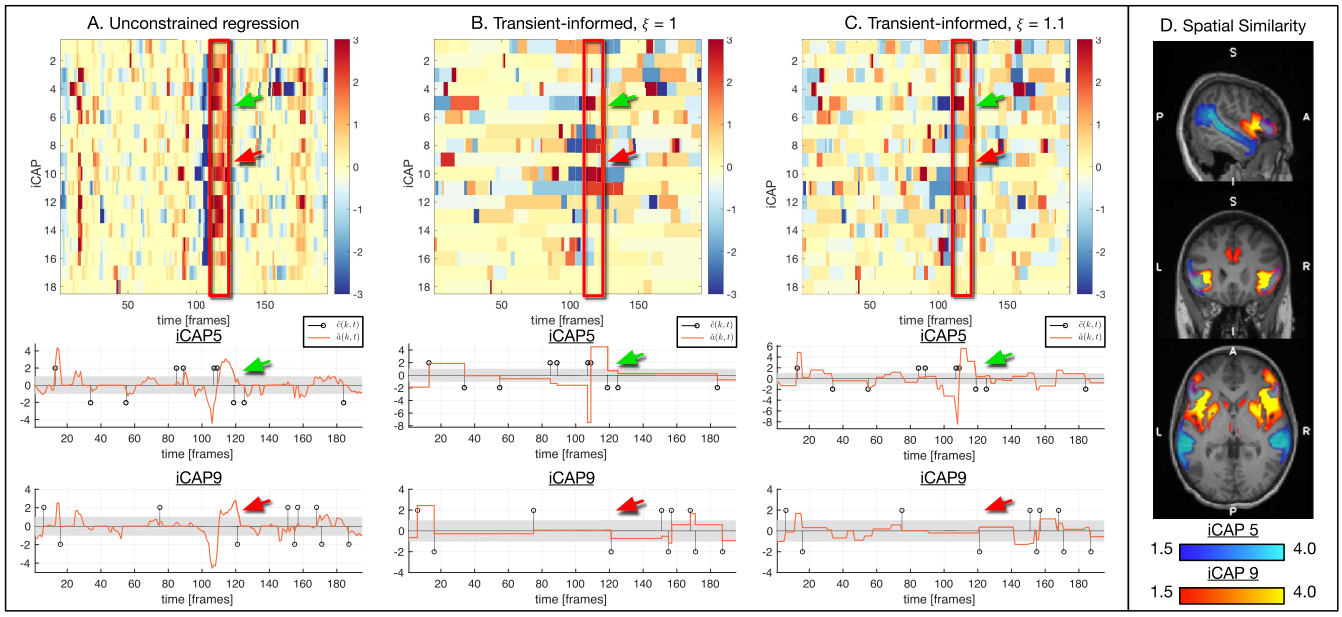

Fig. 7. A) Estimates from unconstrained regression for one exemplary subject. Top plots show time courses $\tilde{a}(\cdot, t)$ for all 18 iCAPs and bottom plots show time courses of iCAP 5 and 9 with their transient indicator functions $\tilde{c}_{\xi=1}(5, \cdot)$ and $\tilde{c}_{\xi=1}(9, \cdot)$. The activation threshold z-score $|1|$ is shown as grey background. $\tilde{a}(9, \cdot)$ contains activity which is not seen in $\tilde{c}_{\xi=1}(9, \cdot)$ (red arrow). Changes in $\tilde{a}(5, \cdot)$ correspond better to transient locations (green arrow). B) Transient-informed regression at $\xi = 1$ yields a better correspondence between time courses $\tilde{a}(k, \cdot)$ and transients $\tilde{c}_{\xi=1}(k, \cdot)$, but contain very sparse, biologically unlikely activations. C) Transient-informed regression at optimum $\xi = 1.1$ still suppresses unlikely activations such as in iCAP 9 (red arrow), but allows multiple iCAPs to change simultaneously and leads to smoother time courses. D) There is significant spatial overlap between iCAP 5 and iCAP 9, which may have introduced the artifacts seen in the time course of iCAP 9 using unconstrained regression.

estimated innovations was 0.96. As an alternative, we also used the Bayesian Information Criterion (BIC) to evaluate different soft assignment factors. In this case, the optimum factor at the knee point of the curve was $\xi = 1.25$.

We also evaluated ξ on simulated data to validate the quality measures we used here (see Supplementary Fig. S3, available in the supplementary files/multimedia tab). These evaluations on simulated data indicate that both correlation and BIC are good measures to estimate the optimum soft assignment factor ξ.

E. Experimental Data: Qualitative Evaluation and Temporal Overlap

In Fig. 7, we show recovered time courses for one exemplary subject. In unconstrained regression results (Fig. 7A), there appear segments where almost all iCAPs are found active at the same time (e.g., red box). When comparing the estimated activations $\tilde{\mathbf{A}}$ with transient timings $\tilde{\mathbf{C}}_{\xi=1}$, significant differences (here represented for iCAP 9, red arrow) become evident. With transient-informed regression at $\xi = 1$ (Fig. 7B), time course changes are restricted to timepoints at a-priori known transient timepoints, which leads to a better correspondence between the transitions of $\tilde{\mathbf{A}}$ and $\tilde{\mathbf{C}}$. It is to note that signs of estimated transients of time courses $\tilde{\mathbf{a}}(k, \cdot)$ correspond well with the iCAP signs of $\tilde{\mathbf{c}}(k, \cdot)$, even though this was not explicitly imposed by the algorithm. However, for $\xi = 1$ activation changes are very sparse, suggesting that hard cluster assignment is a too restrictive constraint in the time course estimation. With transient-informed regression at optimum $\xi = 1.1$ (Fig. 7C), activations still correspond very well with transient timings, suppressing activations that are most likely wrong (as in iCAP 9, red arrow). Yet, retrieved signals are more smooth and multiple iCAPs can change at the same time. The probably falsely detected activations retrieved during unconstrained regression may have been introduced by spatial dependence between the iCAPs (Fig. 7D).

To investigate differences in the whole group, we computed temporal overlap and total activity duration in every subject and compared the results for the different regression approaches. Again, time courses were thresholded at an absolute z-score of 1 to find activity timepoints. Across subjects, temporal overlap in unconstrained regression and transient-informed regression at $\xi = 1$ revealed 3.06 ± 0.36 and 3.02 ± 0.39 co-active iCAPs on average, respectively. In transient-informed regression at optimal $\xi = 1.1$, temporal overlap was significantly higher with 3.47 ± 0.44 co-active iCAPs on average.

From qualitative observation in single subjects (e.g., Fig. 7), we hypothesized that spatial overlap leads to an over-estimation of co-activations with the same sign in unconstrained estimates. To test for this quantitatively, we computed the percentage of co-activations with the same sign for pairwise combinations of iCAPs (Fig. 8) and correlated these co-activation occurrences with spatial Jaccard similarity (subsection IV-B). In unconstrained regression, 85.99 % of all pairwise iCAPs co-activations had the same sign, while in transient-informed regression this was only the case in 45.99 % ($\xi = 1$) and 47.56 % ($\xi = 1.1$) of co-activations. Correlation of the percentage of same-signed co-activations with Jaccard similarity was very high for

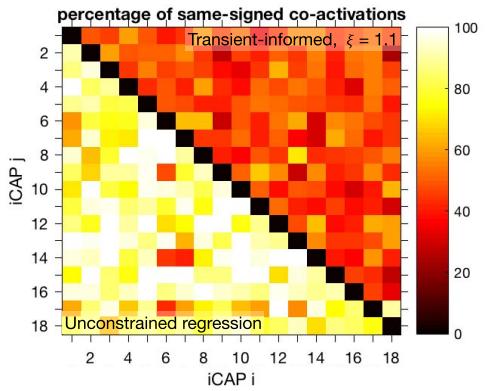

Fig. 8. Percentage of appearances with the same sign for pairwise co-occurrences of iCAPs in unconstrained regression (below diagonal) and in transient-informed regression with $\xi = 1.1$ (above diagonal). In unconstrained regression estimates, iCAPs appear mostly with the same sign.

unconstrained regression ($\rho = 0.54$, $p < 0.001$), almost zero ($\rho = 0.09$, $p = 0.27$) for $\xi = 1$, and in between the two previous values ($\rho = 0.31$, $p < 0.001$) for optimal $\xi = 1.1$.

As a large confound in fMRI analysis is motion, we conducted an additional analysis to verify whether the over-representation of same-signed co-activations in unconstrained regression might be related to motion artifacts. For this, we computed the overall percentage of same-signed co-activations across all pairwise iCAPs combinations for each subject and then calculated the correlation across subjects between this measure and the average framewise displacement. There was a tendency relationship in unconstrained regression ($\rho = 0.26$, $p = 0.05$) suggesting that in subjects with higher motion, there is a higher over-representation of same-signed co-activations. In transient-informed regression this relationship was entirely corrected, both for $\xi = 1$ ($\rho = -0.01$, $p = 0.93$) and for $\xi = 1.1$ ($\rho = 0.02$, $p = 0.86$).

V. Discussion

FMRI is one unique tomographic imaging modality to observe the brain at work in a non-invasive way, however, the rich structure of the data requires advanced analysis methods. The iCAPs framework combines two main ingredients: first, the TA deconvolution with regularization that drives sparse innovation signals; and, second, temporal clustering of fMRI frames with strong innovations. As temporal clustering allows for spatial overlap of the iCAPs maps, the recovery of the associated time courses from activity-inducing signals can be impeded if a timepoint-wise spatial regression is used to which we refer as unconstrained regression. We observed this effect not only qualitatively in iCAPs' activity-inducing time courses of single subjects (e.g., Fig. 7A, red box), but we also confirmed it quantitatively in simulated and experimental data. In particular, iCAPs appeared significantly more with the same sign (activated vs de-activated) when using the unconstrained regression. The high correlation between measures of spatial and temporal overlap further corroborates that without the use of additional constraints, temporal co-activation caused by spatial dependencies cannot be well differentiated from true underlying co-activation. The contribution of this work is to exploit the additional information that is available from the TA deconvolution procedure; i.e., innovations that encode moments of transient activity—information that can be advantageously incorporated in a spatio-temporal regression procedure for more consistent results. The recovered activity-inducing signals then play a crucial role in evaluating more general measures, for instance, iCAPs configurations of temporal overlap [23] or more advanced temporal models; e.g., hidden Markov models [35].

Applied on simulated data with known timepoints of transient activity, the proposed approach performed significantly better in recovering block-like time courses than unconstrained regression, both in terms of estimation error and estimated temporal overlap between networks. We demonstrated that temporal overlap between networks is consistently underestimated by unconstrained regression, while there is no such systematic bias in transient-informed estimates. This bias is towards same-signed co-activations in unconstrained estimates. These results show that the new procedure exploits well the additional information (i.e., transient timepoints) that is available in the simulated setting as ground truth.

For the experimental results, we applied the iCAPs framework on a sample of 56 healthy subjects. We observed significant spatial overlap between 26 % of retrieved iCAPs maps. Higher spatial similarity was mainly observed in networks containing posterior regions (posterior cingulate and visual networks), which confirms observations by [23] of high spatial overlap mainly in posterior regions. Spatial overlap is clearly a feature of resting-state networks when allowed for. We then used soft cluster assignment of transient frames to account for the fact that ground truth transients are not known. The optimal factor for soft cluster assignment was of similar scale if evaluated in terms of correspondence between measured and estimated transients ($\xi = 1.1$) and in terms of BIC ($\xi = 1.25$), which was also confirmed in simulations (see Supplementary Fig. S3, available in the supplementary files/multimedia tab). For $\xi = 1.1$, the correlation between spatial and temporal overlap was still significant, but substantially lower than in unconstrained regression. However, the estimated percentage of same-signed co-activations was only slightly higher than for the most restrictive case $\xi = 1$ and substantially lower than in the unconstrained case. Together, these results suggest that even though the interaction between spatial and temporal overlap could not be completely avoided, false temporal co-activations due to spatial dependence, as indicated by an over-representation of same-sign co-activations, could be significantly reduced. Furthermore, motion-related effects on the sign of co-activations were entirely removed in transient-informed regression.

Transient-informed regression can be related to more general nonlinear regression methods such as segmented regression, spline regression in the case of piecewise polynomial functions [36], and locally weighted regression [37], [38]. In those cases, the input space is decomposed in (usually uniformly distributed) sub-parts, and independent regressions are applied to each of them. A large body of literature also exists

on the estimation of breakpoints in a segmented regression problem (see [39], [40]). Approaches inspired by this principle have been applied in neuroimaging; e.g., dynamic connectivity regression (DCR) [19], which detects change points of FC by subsequently sub-dividing the time courses in windows with variable length. While segmented regression methods either assume equally spaced change points or estimate the optimum change points from the data, in the present work, change points are not estimated during regression, but taken from the transients that are revealed by the deconvolution and derivative in the previous processing steps. Further, it is to note that most segmented regression approaches apply the same change points to the whole brain while in the present work, we extract and apply change points that are *specific* to each network, which allows for a high flexibility in retrieving independent time courses for each network. In addition to change points, a second piece of information is taken from previous processing steps: the spatial information of the iCAPs maps is used to group voxels and, therefore, both spatial and temporal constraints are included in a single spatio-temporal regression. Since change points are defined based on transients and no second-order correlations need to be computed, the approach overcomes limitations related to the selection of the window size for dFC calculation. Furthermore, it allows to recover temporal overlap, which is not possible in change point detection approaches that are based on temporal subdivision into windows [19], [41] or in point process approaches that only detect co-activation of brain regions [15]–[17]. We also mention the more recent use of temporal ICA [42] for fMRI data. Here, temporal statistical independence is favored, but since there is no derivative involved, temporal overlap can as well not be accounted for, and thus the method has only been deployed for fast-TR and long acquisitions.

The iCAPs approach is also closely related to other methodologies that allow networks to be temporally overlapping. The probably most widely used such methodology to date is ICA that relies on a surrogate measure for statistical independence [4]. Conventional ICA for fMRI deploys this criterion in the spatial domain due to the dimensionality of the data ($N_v \gg N_t$) and concatenates all subjects' data in the temporal dimension. Therefore, the estimated sources at the group level are spatial maps and the recovery of the individuals' time courses is required, for which three main approaches have emerged [43], [44]. First, back-reconstruction [4] of temporal principal component analysis (PCA) reduced data recovers time courses by applying the inverse PCA projections. Second, the dual regression technique [45] uses the group-level maps as regressors on the individual complete functional data. The obtained time courses are then normalized and used on their turn as regressors to obtain individual maps. Third, spatially constrained ICA [44] relies on a similar approach for time course recovery, but estimates individual maps first and then uses them as regressors on the individual BOLD signals for each subject separately. In the latter two approaches, time courses are basically recovered by spatial regression for each timepoint, which is essentially the same procedure as in the original iCAPs framework [24] that we called "unconstrained regression" in the current paper. Similar to iCAPs, these ICA-based approaches allow to recover temporal overlap of brain networks (see [46]). Contrary to ICs, iCAPs can be spatially correlated (see also Supplementary Figs. S4 and S5, available in the supplementary files/multimedia tab), which requires the introduction of constraints for the successful recovery of temporal overlap as proposed in the current paper. When accounted for this artifact, the iCAPs framework is unique in its ability to give access to spatially *and* temporally overlapping brain networks.

It is noteworthy that statistical dependence is not equivalent to spatial overlap; i.e., spatial ICs being uncorrelated does not necessarily mean that they cannot contain spatial overlap [47], [48]. However, overlapping areas in ICs mostly appear with different sign to ensure that the maps are spatially uncorrelated. In practice, ICs appear thus either spatially segregated or introduce negativity, which impedes interpretability. Additionally, ICA is based on a source separation model that does not explicitly include a noise term and consequently, ICs of interest have to be visually inspected and selected, whereas TA already includes denoising and deconvolution. With the iCAPs framework, we found multiple networks including the posterior cingulate cortex that do not only include the DMN [23], an observation that had never been revealed before.

From a neuroscientific perspective, the present results support the view of functional networks of distributed brain regions that co-activate with substantial temporal overlap. Our results further improve the iCAPs approach with better and more robust time course recovery. The fact that iCAPs seem to co-activate and -deactivate in approximately a balanced way corroborates recent findings using other methodologies. For instance, dominant spatial patterns of voxel-wise sliding-window dFC are characterized by roughly task-negative versus-positive networks, however, with notable subsystems of each network that change side [49]. The organization of the brain in two opposing networks has also been explained using topographic principles on the cortical surface derived from resting-state FC [50]. Similar dynamic behavior was reported by [51] using graph-based FC and measures of modular network organization. In terms of potential applications, dynamic analysis of large-scale brain networks is of high interest in the investigation of brain development with age (as demonstrated, for example, in [52]–[56]). In section S1. Supplementary Results (available in the supplementary files/multimedia tab), we show that temporal properties of iCAPs retrieved with the method proposed here are correlated with age, which further supports the relevance of dynamic network activity for development. Other applications of interest include the investigation of the relationship between brain function and cognition [57], or in the search for alterations and biomarkers in clinical populations (e.g., in patients with schizophrenia [58], autism [59], or Alzheimer's disease [60]). Finally, the proposed methodology is not restricted to the analysis of resting-state data since task-based paradigms can also be analyzed, which is of particular interest when probing into functional brain mechanisms related to cognition and behavioral performance [57], [61].

VI. Conclusions and Future Directions

We have addressed the crucial step in the iCAPs framework of activity-inducing time course recovery, which is essential to properly quantify temporal overlap of functional brain networks. We showed that the conventional unconstrained regression approach is hindered by spatial dependencies of the iCAPs maps, which cannot be avoided as these maps are spatially overlapping and not orthogonal. We therefore have introduced a transient-informed spatio-temporal regression scheme, which incorporates knowledge on transients and finds the activity-inducing signal levels by a global fit. We validated our approach on simulated data and demonstrated its potential on experimental data.

The iCAPs framework is still a fairly new approach for large-scale network retrieval, and even though it is unique in its potential to retrieve spatially *and* temporally overlapping networks, there are still possible improvements that can be made in the framework. First, in the TA step, the HRF deconvolution using TA could possibly be improved by the consideration of a variable HRF model [62]. Second, the selection of the number of clusters for retrieval of iCAPs maps is not unique. Here, we selected $K = 18$ clusters since consensus clustering showed high stability, which was not significantly improved by considering more clusters. However, clustering was also fairly stable for different K. Future work should explicitly address this question by investigating stability and consistency for different numbers of clusters.

Finally, physiological noise such as motion or spontaneous breath hold is always a confounding factor. Here, we used scrubbing and regression of white matter and CSF signals to account for such artifacts. We further demonstrated that the effect of motion on erroneous time course estimation could be corrected by using transient-based constraints. However, further research should investigate whether there is a relationship between all types of physiological noise and the occurrence or co-occurrence of particular networks.

Acknowledgments

The authors thank Dr. Djalel Meskaldji for the insightful discussions and Dr. Younes Farouj for his support in the preparation of an open repository with the full code. Further, they are grateful to the subjects who participated in our study and thank Sarah Menghetti, Léa Chambaz, Virginie Pouillard and Dr. Maude Schneider for their involvement with the participants. They would also like to acknowledge Prof. François Lazeyras and the CIBM group for their support during data collection.

References

[1] J. S. Damoiseaux *et al.*, "Consistent resting-state networks across healthy subjects," *Proc. Nat. Acad. Sci. USA*, vol. 103, no. 37, pp. 13848–13853, 2006.

[2] M. D. Fox, A. Z. Snyder, J. L. Vincent, M. Corbetta, D. C. Van Essen, and M. E. Raichle, "The human brain is intrinsically organized into dynamic, anticorrelated functional networks," *Proc. Nat. Acad. Sci. USA*, vol. 102, no. 27, pp. 9673–9678, 2005. [Online]. Available: http://www.pnas.org/cgi/doi/10.1073/pnas.0504136102

[3] M. J. McKeown *et al.*, "Analysis of fMRI data by blind separation into independent spatial components," *Hum. Brain Mapping*, vol. 6, no. 3, pp. 160–188, 1998.

[4] V. D. Calhoun, T. Adali, G. D. Pearlson, and J. J. Pekar, "A method for making group inferences from functional MRI data using independent component analysis," *Hum. Brain Mapping*, vol. 14, no. 3, pp. 140–151, 2001.

[5] C. Chang and G. H. Glover, "Time–frequency dynamics of resting-state brain connectivity measured with fMRI," *NeuroImage*, vol. 50, no. 1, pp. 81–98, 2010, doi: 10.1016/j.neuroimage.2009.12.011.

[6] K. Christoff, Z. C. Irving, K. C. R. Fox, R. N. Spreng, and J. R. Andrews-Hanna, "Mind-wandering as spontaneous thought: A dynamic framework," *Nature Rev. Neurosci.*, vol. 17, pp. 718–731, Sep. 2016, doi: 10.1038/nrn.2016.113.

[7] M. G. Preti, T. A. W. Bolton, and D. Van De Ville, "The dynamic functional connectome: State-of-the-art and perspectives," *Neuroimage*, vol. 160, pp. 41–54, Oct. 2017.

[8] F. I. Karahanoğlu and D. Van De Ville, "Dynamics of large-scale fMRI networks: Deconstruct brain activity to build better models of brain function," *Current Opinion Biomed. Eng.*, vol. 3, pp. 28–36, Sep. 2017. [Online]. Available: http://linkinghub.elsevier.com/retrieve/pii/S2468451117300417

[9] R. M. Hutchison *et al.*, "Dynamic functional connectivity: Promise, issues, and interpretations," *Neuroimage*, vol. 80, pp. 360–378, Oct. 2013, doi: 10.1016/j.neuroimage.2013.05.079.

[10] Ü. Sakoğlu, G. D. Pearlson, K. A. Kiehl, Y. M. Wang, A. M. Michael, and V. D. Calhoun, "A method for evaluating dynamic functional network connectivity and task-modulation: Application to schizophrenia," *Magn. Reson. Mater. Phys., Biol. Med.*, vol. 23, nos. 5–6, pp. 351–366, 2010.

[11] N. Leonardi *et al.*, "Principal components of functional connectivity: A new approach to study dynamic brain connectivity during rest," *Neuroimage*, vol. 83, pp. 937–950, Dec. 2013, doi: 10.1016/j.neuroimage.2013.07.019.

[12] E. A. Allen, E. Damaraju, S. M. Plis, E. B. Erhardt, T. Eichele, and V. D. Calhoun, "Tracking whole-brain connectivity dynamics in the resting state," *Cerebral Cortex*, vol. 24, no. 3, pp. 663–676, 2014.

[13] M. Yaesoubi, T. Adalı, and V. D. Calhoun, "A window-less approach for capturing time-varying connectivity in fMRI data reveals the presence of states with variable rates of change," *Hum. Brain Mapping*, vol. 39, no. 4, pp. 1626–1636, 2018.

[14] D. Vidaurre, S. M. Smith, and M. W. Woolrich, "Brain network dynamics are hierarchically organized in time," *Proc. Nat. Acad. Sci. USA*, vol. 114, no. 48, pp. 12827–12832, 2017. [Online]. Available: http://www.pnas.org/lookup/doi/10.1073/pnas.1705120114

[15] E. Tagliazucchi, P. Balenzuela, D. Fraiman, and D. R. Chialvo, "Criticality in large-scale brain fMRI dynamics unveiled by a novel point process analysis," *Front. Physiol.*, vol. 3, p. 15, Feb. 2012.

[16] X. Liu and J. H. Duyn, "Time-varying functional network information extracted from brief instances of spontaneous brain activity," *Proc. Nat. Acad. Sci. USA*, vol. 110, no. 11, pp. 4392–4397, 2013. [Online]. Available: http://www.pnas.org/cgi/doi/10.1073/pnas.1216856110 and http://www.pubmedcentral.nih.gov/articlerender.fcgi?artid=3600481&tool=pm%centrez&rendertype=abstract

[17] X. Liu, C. Chang, and J. H. Duyn, "Decomposition of spontaneous brain activity into distinct fMRI co-activation patterns," *Front. Syst. Neurosci.*, vol. 7, p. 101, Dec. 2013. [Online]. Available: http://journal.frontiersin.org/article/10.3389/fnsys.2013.00101/abstrac%t

[18] E. Tagliazucchi, M. Siniatchkin, H. Laufs, and D. R. Chialvo, "The voxel-wise functional connectome can be efficiently derived from co-activations in a sparse spatio-temporal point-process," *Front. Neurosci.*, vol. 10, p. 381, Aug. 2016.

[19] I. Cribben, R. Haraldsdottir, L. Y. Atlas, T. D. Wager, and M. A. Lindquist, "Dynamic connectivity regression: Determining state-related changes in brain connectivity," *NeuroImage*, vol. 61, no. 4, pp. 907–920, 2012, doi: 10.1016/j.neuroimage.2012.03.070.

[20] J. M. Shine, O. Koyejo, P. T. Bell, K. J. Gorgolewski, M. Gilat, and R. A. Poldrack, "Estimation of dynamic functional connectivity using multiplication of temporal derivatives," *NeuroImage*, vol. 122, pp. 399–407, Nov. 2015, doi: 10.1016/j.neuroimage.2015.07.064.

[21] J. M. Shine, O. Koyejo, and R. A. Poldrack, "Temporal metastates are associated with differential patterns of time-resolved connectivity, network topology, and attention," *Proc. Nat. Acad. Sci. USA*, vol. 113, no. 35, pp. 9888–9891, 2016. [Online]. Available: http://www.pnas.org/lookup/doi/10.1073/pnas.1604898113

[22] J. M. Shine *et al.*, "The dynamics of functional brain networks: Integrated network states during cognitive task performance," *Neuron*, vol. 92, no. 2, pp. 544–554, 2016.

[23] F. I. Karahanoğlu and D. Van De Ville, "Transient brain activity disentangles fMRI resting-state dynamics in terms of spatially and temporally overlapping networks," *Nature Commun.*, vol. 6, Jul. 2015, Art. no. 7751. [Online]. Available: http://www.nature.com/doifinder/10.1038/ncomms8751

[24] F. I. Karahanoğlu, C. Caballero-Gaudes, F. Lazeyras, and D. Van De Ville, "Total activation: FMRI deconvolution through spatio-temporal regularization," *NeuroImage*, vol. 73, pp. 121–134, Jun. 2013.

[25] Y. Farouj, F. I. Karahanoğlu, and D. Van De Ville, "Regularized spatiotemporal deconvolution of fMRI data using gray-matter constrained total variation," in *Proc. 14th IEEE Int. Symp. Biomed. Imag.*, Apr. 2017, pp. 472–475.

[26] I. Khalidov, J. Fadili, F. Lazeyras, D. Van De Ville, and M. Unser, "Activelets: Wavelets for sparse representation of hemodynamic responses," *Signal Process.*, vol. 91, no. 12, pp. 2810–2821, 2011.

[27] R. B. Buxton, E. C. Wong, and L. R. Frank, "Dynamics of blood flow and oxygenation changes during brain activation: The balloon model," *Magn. Reson. Med.*, vol. 39, no. 6, pp. 855–864, 1998.

[28] F. I. Karahanoğlu, I. Bayram, and D. Van De Ville, "A signal processing approach to generalized 1-D total variation," *IEEE Trans. Signal Process.*, vol. 59, no. 11, pp. 5265–5274, Nov. 2011.

[29] J. Ashburner, "A fast diffeomorphic image registration algorithm," *NeuroImage*, vol. 38, no. 1, pp. 95–113, 2007.

[30] S. Monti, P. Tamayo, J. Mesirov, and T. Golub, "Consensus clustering: A resampling-based method for class discovery and visualization of gene expression microarray data," *Mach. Learn.*, vol. 52, no. 1, pp. 91–118, 2003.

[31] J. D. Power, K. A. Barnes, A. Z. Snyder, B. L. Schlaggar, and S. E. Petersen, "Spurious but systematic correlations in functional connectivity MRI networks arise from subject motion," *NeuroImage*, vol. 59, no. 3, pp. 2142–2154, 2012, doi: 10.1016/j.neuroimage.2011.10.018.

[32] Y. Chao-Gan and Z. Yu-Feng, "DPARSF: A MATLAB toolbox for 'pipeline' data analysis of resting-state fMRI," *Frontiers Syst. Neurosci.*, vol. 4, p. 13, May 2010.

[33] Y. Alemán-Gómez, L. Melie-García, and P. Valdés-Hernandez, "IBASPM: Toolbox for automatic parcellation of brain structures," Presented at the 12th Annu. Meeting Org. Hum. Brain Mapping, Florence, Italy, vol. 27, no. 1, Jun. 2006.

[34] J. Ashburner and K. J. Friston, "Unified segmentation," *NeuroImage*, vol. 26, no. 3, pp. 839–851, 2005.

[35] T. A. W. Bolton, A. Tarun, V. Sterpenich, S. Schwartz, and D. Van De Ville, "Interactions between large-scale functional brain networks are captured by sparse coupled HMMs," *IEEE Trans. Med. Imag.*, vol. 37, no. 1, pp. 230–240, Jan. 2018.

[36] E. J. Wegman and I. W. Wright, "Splines in statistics," *J. Amer. Stat. Assoc.*, vol. 78, no. 382, pp. 351–365, 1983.

[37] W. S. Cleveland and S. J. Devlin, "Locally weighted regression: An approach to regression analysis by local fitting," *J. Amer. Stat. Assoc.*, vol. 83, no. 403, pp. 596–610, 1988. [Online]. Available: http://www.jstor.org/stable/2289282%5Cnhttp://about.jstor.org/terms

[38] C. G. Atkeson, A. W. Moore, and S. Schaal, "Locally weighted learning for control," *Artif. Intell. Rev.*, vol. 11, nos. 1–5, pp. 75–113, 1997.

[39] J. Acharya, I. Diakonikolas, J. Li, and L. Schmidt, "Fast algorithms for segmented regression," in *Proc. 33rd Int. Conf. Mach. Learn.*, vol. 48, Jul. 2016, pp. 2878–2886. [Online]. Available: http://proceedings.mlr.press/v48/acharya16.html

[40] Y. Yamamoto and P. Perron, "Estimating and testing multiple structural changes in linear models using band spectral regressions," *Econometrics J.*, vol. 16, no. 3, pp. 400–429, 2013.

[41] Y. Xu and M. A. Lindquist, "Dynamic connectivity detection: An algorithm for determining functional connectivity change points in fMRI data," *Frontiers Neurosci.*, vol. 9, p. 285, Sep. 2015.

[42] S. M. Smith *et al.*, "Temporally-independent functional modes of spontaneous brain activity," *Proc. Nat. Acad. Sci. USA*, vol. 109, no. 8, pp. 3131–3136, 2012. [Online]. Available: http://www.ncbi.nlm.nih.gov/pubmed/22323591

[43] E. B. Erhardt, S. Rachakonda, E. J. Bedrick, E. A. Allen, T. Adali, and V. D. Calhoun, "Comparison of multi-subject ICA methods for analysis of fMRI data," *Hum. Brain Mapping*, vol. 32, no. 12, pp. 2075–2095, 2011.

[44] Y. Du, E. A. Allen, H. He, J. Sui, L. Wu, and V. D. Calhoun, "Artifact removal in the context of group ICA: A comparison of single-subject and group approaches," *Hum. Brain Mapping*, vol. 37, no. 3, pp. 1005–1025, 2016.

[45] C. F. Beckmann, C. E. Mackay, N. Filippini, and S. M. Smith, "Group comparison of resting-state FMRI data using multi-subject ICA and dual regression," *Neuroimage*, vol. 47, p. S148, Jun. 2009.

[46] R. L. Miller *et al.*, "Higher dimensional meta-state analysis reveals reduced resting fMRI connectivity dynamism in schizophrenia patients," *PLoS One*, vol. 11, no. 3, p. e0149849, 2016.

[47] I. Daubechies *et al.*, "Independent component analysis for brain fMRI does not select for independence," *Proc. Nat. Acad. Sci. USA*, vol. 106, no. 26, pp. 10415–10422, 2009.

[48] V. D. Calhoun *et al.*, "Independent component analysis for brain fMRI does indeed select for maximal independence," *PLoS One*, vol. 8, no. 8, p. e73309, 2013.

[49] M. G. Preti and D. Van De Ville, "Dynamics of functional connectivity at high spatial resolution reveal long-range interactions and fine-scale organization," *Sci. Rep.*, vol. 7, no. 1, 2017, Art. no. 12773, doi: 10.1038/s41598-017-12993-1.

[50] D. S. Margulies *et al.*, "Situating the default-mode network along a principal gradient of macroscale cortical organization," *Proc. Nat. Acad. Sci. USA*, vol. 113, no. 44, pp. 12574–12579, 2016.

[51] A. Zalesky, A. Fornito, L. Cocchi, L. L. Gollo, and M. Breakspear, "Time-resolved resting-state brain networks," *Proc. Nat. Acad. Sci. USA*, vol. 111, no. 28, pp. 10341–10346, 2014. [Online]. Available: http://www.pnas.org/content/early/2014/06/25/1400181111

[52] R. M. Hutchison and J. B. Morton, "Tracking the brain's functional coupling dynamics over development," *J. Neurosci.*, vol. 35, no. 17, pp. 6849–6859, 2015. [Online]. Available: http://www.jneurosci.org/cgi/doi/10.1523/JNEUROSCI.4638-14.2015

[53] J. Qin *et al.*, "Predicting individual brain maturity using dynamic functional connectivity," *Frontiers Hum. Neurosci.*, vol. 9, p. 418, Jul. 2015. [Online]. Available: http://journal.frontiersin.org/Article/10.3389/fnhum.2015.00418/abstrac%t

[54] R. M. Hutchison and J. B. Morton, "It's a matter of time: Reframing the development of cognitive control as a modification of the brain's temporal dynamics," *Develop. Cogn. Neurosci.*, vol. 18, pp. 70–77, Apr. 2016, doi: 10.1016/j.dcn.2015.08.006.

[55] S. Ryali *et al.*, "Temporal dynamics and developmental maturation of salience, default and central-executive network interactions revealed by variational bayes hidden Markov modeling," *PLoS Comput. Biol.*, vol. 12, no. 12, p. e1005138, 2016. [Online]. Available: http://dx.plos.org/10.1371/journal.pcbi.1005138

[56] R. P. Viviano, N. Raz, P. Yuan, and J. S. Damoiseaux, "Associations between dynamic functional connectivity and age, metabolic risk, and cognitive performance," *Neurobiol. Aging*, vol. 59, pp. 135–143, Nov. 2017, 10.1016/j.neurobiolaging.2017.08.003.

[57] J. R. Cohen, "The behavioral and cognitive relevance of time-varying, dynamic changes in functional connectivity," *NeuroImage*, vol. 180, pp. 515–525, Oct. 2018, doi: 10.1016/j.neuroimage.2017.09.036.

[58] E. Damaraju *et al.*, "Dynamic functional connectivity analysis reveals transient states of dysconnectivity in schizophrenia," *NeuroImage, Clin.*, vol. 5, pp. 298–308, Jul. 2014, [Online]. Available: https://www.sciencedirect.com/science/article/pii/S2213158214000953, doi: 10.1016/j.nicl.2014.07.003.

[59] C.-Y. Wee, P.-T. Yap, and D. Shen, "Diagnosis of autism spectrum disorders using temporally distinct resting-state functional connectivity networks," *CNS Neurosci. Therapeutics*, vol. 22, no. 3, pp. 212–219, 2016. [Online]. Available: http://doi.wiley.com/10.1111/cns.12499

[60] A. Córdova-Palomera *et al.*, "Disrupted global metastability and static and dynamic brain connectivity across individuals in the Alzheimer's disease continuum," *Sci. Rep.*, vol. 7, Jan. 2017, Art. no. 40268. [Online]. Available: http://www.nature.com/articles/srep40268

[61] J. D. Medaglia, M.-E. Lynall, and D. S. Bassett, "Cognitive network neuroscience," *J. Cogn. Neurosci.*, vol. 27, no. 8, pp. 1471–1491, 2015.

[62] D. Rangaprakash, G.-R. Wu, D. Marinazzo, X. Hu, and G. Deshpande, "Hemodynamic response function (HRF) variability confounds resting-state fMRI functional connectivity," *Magn. Reson. Med.*, vol. 80, no. 4, pp. 1697–1713, 2018. [Online]. Available: http://doi.wiley.com/10.1002/mrm.27146